Journal of Fluids and Structures 65 (2016) 121–137

Contents lists available at ScienceDirect

Journal of Fluids and Structures

journal homepage: www.elsevier.com/locate/jfs

Dynamic leg-motion and its effect on the aerodynamic performance of cyclists

Timothy N. Crouch [a,*], David Burton [a], Mark C. Thompson [a], Nicholas A.T. Brown [b], John Sheridan [a]

[a] Fluids Laboratory for Aeronautical and Industrial Research (FLAIR), Department of Mechanical and Aerospace Engineering, Monash University, Clayton, VIC 3800, Australia
[b] Australian Institute of Sport, Belconnen, Canberra 2616, Australia

ARTICLE INFO

Article history:
Received 24 September 2015
Received in revised form
10 May 2016
Accepted 17 May 2016
Available online 4 June 2016

Keywords:
Sports aerodynamics
Wakes
Vortex structures
Bluff-body flows

ABSTRACT

In this wind-tunnel based experimental study, the flow topology of the near wake of a generic anatomically accurate model cyclist is mapped for a range of reduced pedalling frequencies. Wake flow fields for both static leg and pedalling cyclists are compared over the full 360° rotation of the crank using both time- and phase-averaging. The primary wake flow structures and aerodynamic forces are quantified and analysed under dynamic pedalling conditions representative of an elite-level time-trial cyclist. Over the range of reduced pedalling frequencies studied, only minor variation was detected between the instantaneous drag and primary vortical structures of a pedalling cyclist compared to a stationary cyclist with the pedals in the same position. A simplified model of the aerodynamic forces acting on the legs under motion is presented to provide insight into how the motion of the legs influences aerodynamic drag. A comparison of predicted forces from this model with those from experiments provides a new perspective on how the aerodynamics of cyclists may be optimised.

1. Introduction

At the elite level optimising the aerodynamics of the bicycle-rider system is one of the most efficient and effective ways to reduce race times. Practically, the drive to minimise aerodynamic drag can be seen in the extreme aerodynamic positions of time-trial cyclists, the geometry and drag-reducing surface finishes of the equipment they use, race tactics employing drafting, and the significant resources that leading nations and teams devote to improving the aerodynamics of their athletes. Looking forward, further gains in cycling performance are likely to arise from an improved fundamental understanding of the governing fluid mechanisms and universal principles that can enhance aerodynamics.

Advances in our understanding of three-dimensional flows around cyclist geometries have led to a new outlook on how to improve cycling technologies (Hosoi, 2014). Similarly, many other sports have also benefited immensely from insight gained into the fundamental fluid mechanisms that play a governing role in sporting performance, most notably for automobile racing, swimming and ball/projectile-type sports (Katz, 2006; Wei et al., 2014; Clanet, 2015). For cycling, recent experimental and numerical investigations by Crouch et al. (2014a) and Griffith et al. (2014) have provided insight into the

* Corresponding author.
E-mail address: timothy.crouch@monash.edu (T.N. Crouch).

http://dx.doi.org/10.1016/j.jfluidstructs.2016.05.007
0889-9746/

nature of the dominant fluid mechanisms influencing aerodynamics. These investigations employed a quasi-steady analysis, whereby the large-scale flow structures that develop in the wake were characterised as a function of static leg position around a full 360° revolution of the crank. Specific induced changes to the wake structure as leg position was varied were related to large changes in aerodynamic drag (varying by up to 20%) and surface pressures acting on the cyclist's body. The major flow structure variants, broadly characterised by symmetrical and asymmetrical wakes, were associated with low- and high-drag states, respectively. The low-drag (symmetrical) flow regime occurred for crank angles with the pedals lying in a near horizontal plane, which also corresponded to close alignment of the upper thighs of both legs. The high-drag (asymmetrical) wake state was found for crank angles with one leg raised and the other in an extended position.

Although these investigations provide a good starting point for considering the effects of leg position on the aerodynamics, the next logical step is to explicitly include the effect of leg motion on the fluid dynamics. To date the majority of investigations of the flow around cyclist geometries have only considered static leg positions or time-averaged aerodynamic flow quantities in the wake of pedalling cyclists (Barry et al., 2014; Defraeye et al., 2010). This current understanding of a quasi-steady cyclist wake is thought to provide a reasonable approximation of time-varying flows around cyclists, as the time-scale associated with leg motion is relatively large compared with that of the bulk fluid motion for practical cycling speeds and cadences. However at some point, as the pedalling frequency is increased for a given riding speed, this assumption will no longer hold.

There is a possibility that the motion of the legs will couple with the wake in some nonlinear manner resulting in changes to the wake structure and aerodynamic forces with increased pedalling frequency. These could present themselves as alterations to the size, strength and phase of the characteristic wake flow structures, or a complete reorganisation of the wake structure through significant modifications to the location of separation lines from the rider's body. On this point, it is interesting to note that the typical Reynolds numbers applicable to body components at race speeds are close to that of the drag crisis for a circular cylinder. As the leg motion is aligned in a plane with the freestream direction, the cycling of the legs will have a direct effect on the local magnitude of the relative velocity at the leg surface in the direction of the aerodynamic drag force. This will not only induce local changes in velocity at the legs but will also influence the local Reynolds number. The angular and translational accelerations of the legs around the crank cycle will also provide a secondary means for the generation of vorticity at the surfaces of the legs. A primary feature of the cyclist wake with its complex bluff body geometry is the formation of large trailing streamwise vortices. Additional vorticity sources have the potential to add to the strength or decrease the magnitude of these large-scale structures, perhaps affecting induced drag. The leg motion will also induce other inertial effects such as the 'squeezing' and local convective acceleration of fluid between body parts as they come in close proximity to one another, such as the back of the knee and hip joint areas.

This study follows on from the quasi-steady investigation of Crouch et al. (2014a) by providing a detailed analysis of the large-scale wake flow structure and aerodynamic forces acting on a dynamic pedalling cyclist for a range of reduced pedalling frequencies. Preliminary findings by our group have suggested that a similar wake structure can be expected when comparing quasi-steady and dynamic pedalling conditions (Crouch et al., 2014b); however, the current study is aimed at quantifying the similarities and differences.

One important measure of the inertial effects of the leg motion on the flow is the reduced pedalling frequency 'k', given by the ratio of the leg speed around the crank to the forward riding speed:

$$k = \frac{2r\pi f}{U_\infty} = \frac{1}{G} \times \frac{r}{R}, \tag{1}$$

where 'U_∞' is the relative free-stream riding speed, 'r' is the crank length and 'f' is the pedalling frequency. For fixed-gear riding conditions in still winds, this term can be simplified and is independent of the pedalling frequency, being only a function of the bicycle gear-ratio 'G', and the ratio of the crank length to rear wheel radius 'R'. Fig. 1 shows typical reduced frequency values of various road and track cycling events based on common bicycle gearing, crank lengths and wheels used in these events. In this investigation *k-space* is explored, between static quasi-steady conditions ($k=0$) to reduced frequencies representative of an elite-level time trialist ($k=0.115$) as indicated by the markers in Fig. 1. In doing so the degree to which the pedalling motion influences the aerodynamic forces and wake structure can be systematically assessed.

2. Experimental method

The main underlying experimental methods, equipment and facilities for investigating the wake structure of the moving-leg model are described in Crouch et al. (2014a). The full-scale model, bicycle frame and cycling equipment, and time-trial position, pictured in Fig. 2(a) are essentially the same as those used in the previous study. Minor modifications have been made to the knees of the model, and the torso angle (15°) has been increased slightly to accommodate stable rotation of the legs at high pedalling frequencies. A nylon/spandex skin covers the knees to limit the impact of the cavity behind this joint on the flow. The leg position is defined by the angle of the crank 'θ'. The zero-degree leg position corresponds to when the crank is in a horizontal position with the left leg in the downstream location. Fig. 2(a) depicts the model in the 15° crank-angle leg position.

Wake velocity field surveys with the moving-leg model were undertaken in the $2.0 \times 2.0\ \mathrm{m}^2$ working section of the

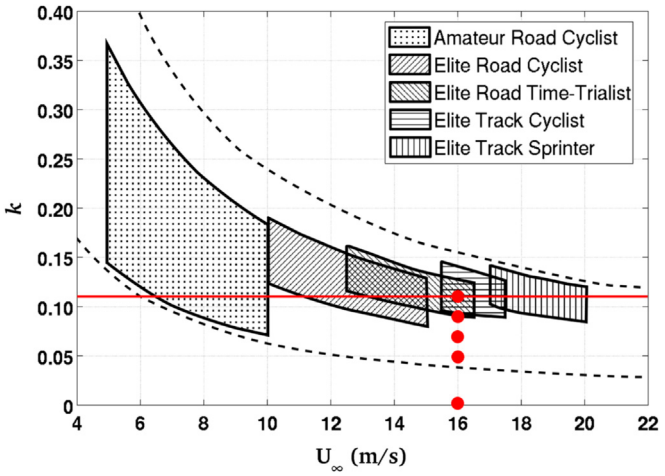

Fig. 1. Typical reduced frequencies of various men and women's road and track cycling events. The area between the dashed lines covers the reduced frequency range for commercially available crank lengths 0.145–0.190 m, and low to high cadence frequencies 0.8–2.0 Hz. The red dots indicate test parameter combinations examined in this paper. (For interpretation of the references to colour in this figure caption, the reader is referred to the web version of this paper.)

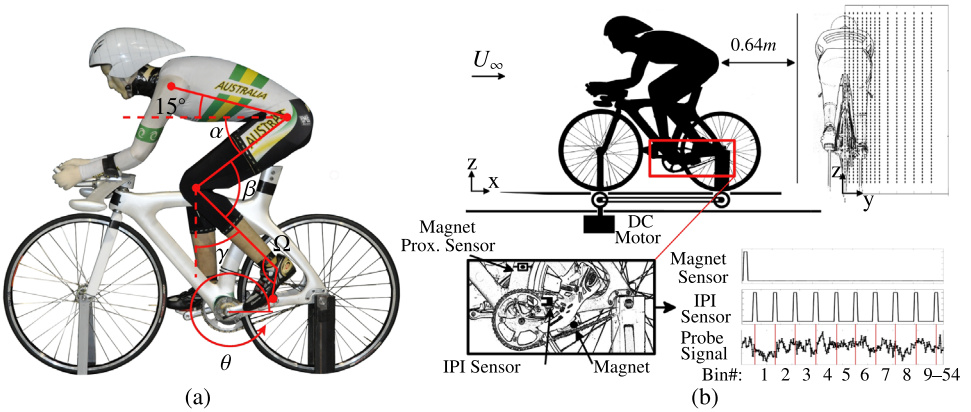

Fig. 2. (a) Model cyclist position and equipment. Hip angle α, knee angle β, lower leg angle γ and ankle angle Ω (fixed for mannequin) are also defined. (b) Wind tunnel setup of the pedalling model. The rear view shows the velocity measurement locations made in a plane one torso length (640 mm) behind the model. The zoomed image of the crank shows the positioning of sensors used to determine the instantaneous angle of the crank. This is shown along with an example depicting the phase-averaging process of probe data using signals output by these sensors.

closed return-circuit 450 kW wind tunnel at Monash University. In this section of the tunnel the free-stream turbulence intensity is measured at <1.4%, with a mean flow uniformity of <1% of U_∞ and angularity of $\pm 1^\circ$. The free-stream test speed was $U_\infty = 16$ m/s, corresponding to a Reynolds number Re of 6.9×10^5 based on the torso length. This was fixed for all reduced pedalling frequencies tested. Wake measurements using a (common) fixed bicycle gear ratio of 4.5:1 are performed at 40, 60, 80 and 100 RPM cadences, which correspond to reduced pedalling frequencies of $k = 0.046$, 0.069, 0.092, and 0.115, respectively. At the 100 RPM cycling cadence, the front and rear wheel ground speed match the wind tunnel free-stream velocity. Velocity fields are also measured for selected static-leg positions representative of the low-drag symmetrical and high-drag asymmetrical flow regimes.

Fig. 2 (b) shows the experimental setup of the model cyclist in the wind tunnel. The model and bicycle are positioned on top of a raised cantilevered platform that reduces the floor boundary layer, and conceals the motor and bicycle wheel drive. The bicycle wheel friction drive consists of a 200 W DC electric motor, which powers rollers connected via a 1:1 belt drive positioned underneath each of the bicycle wheels. Both front and rear wheels, which are fixed on top of the rollers via front- and rear-axle struts, rotate when the rollers are driven. As the rear wheel rotates, the legs are driven around the crank cycle through the fixed gear bicycle drive-train with an accuracy of 0.02 Hz ($\pm$ 1 RPM).

Velocity fields are obtained in a plane normal to the mean flow 0.64 m (one torso length) downstream of the model using a rake of four-hole pressure probes. The rake consisted of four multi-hole pressure probes (Turbulent Flow Instrumentation Pty Ltd) separated by 50 mm that could be accurately positioned in the measurement plane using a motorised two-axis traverse. The response characteristics of these probes have been compared with those from other high frequency velocity measurement techniques, such as hot-wire and laser-Doppler velocimetry. They have been shown to

have a frequency response of up to 2500 Hz (Hooper and Musgrove, 1997; Chen et al., 2000). The probes are capable of measuring all three fluctuating velocity components to within 0.1 m/s and 0.1° for resultant velocity vectors that lie within a $\pm 45°$ forward-facing cone from the probe head.

Fig. 2 (b) shows the locations of probe positions in the wake measurement plane. A total of 780 time sequences of velocity components were taken across one half of the wake at each reduced velocity. The measurements span an area of 0.5×1.3 m^2, starting 0.15 m above the splitter plane so that no velocity measurements resided within the floor boundary layer. The grid resolution covering the core sections of the wake is 25×25 mm^2. Flow symmetry is assumed across the centre-plane of the model for leg positions 180° out-of-phase in order to reconstruct the entire left- and right-hand sides of the wake. This assumption was checked for both static and dynamic leg positions. To check this assumption, velocity measurements spanning the entire width of the wake made at a number of heights (z = 0.3, 0.6, 0.9, 1.2 m). At all points measured velocities for leg positions 180° out-of-phase on the opposite side of the wake were found to be within 5% of U_∞ of each another. Probe measurements have been corrected for solid blockage effects (the blockage of the model is 12.5% based on the effective wind-tunnel cross section with the false floor) based on the methodology of Maskell (1963) to correct reference pitot-static-tube measurements made upstream of the model.

At each measurement location, the time-dependent wake velocity signal of the pedalling mannequin is decomposed using phase-averaging based on leg position. Measurements of crank-angle position were synchronised with the velocity field measurements, as depicted in Fig. 2, allowing the full phase-averaged planar velocity field to be extracted. The crank angle was determined at 54 intervals around the cycle to within ±0.25° using an *Inferred-Photo-Interrupter* (IPI). The IPI was positioned on the bicycle frame so that a pulse signal output was obtained as each tooth (1–54) of the large chain ring passed through the sensor. A magnet proximity sensor fixed to the frame marked the beginning of each crank cycle as a magnet positioned on the crank-arm passed the sensor every revolution. The magnet sensor also served as a method of checking that all 54 pulses were received from the IPI for each crank revolution.

Phase-averaged velocity fields have been constructed by binning cobra-probe data in-between intervals at which the crank angle position was recorded. This corresponds to a bin size of 6.67°. The probe and crank-angle sensors were sampled at a rate of 2500 Hz. The sample time was selected so that the uncertainty 'ϵ' associated with the variability of phase-averaged measurements in each bin was <1.5% of U_∞ at a 95% confidence level. This resulted in a sample duration of 360 s in the most turbulent areas of the wake (below the hips) and 300 s elsewhere (above the hips). For the 100 RPM pedalling frequency, this resulted in phase-averaged measurements recorded over 600 crank cycles. The convergence of the mean phase-averaged result of the streamwise velocity component at a point positioned in a relatively turbulent area of the wake (y=0, z = 0.7 m) is shown in Fig. 3. Sampling times were found to be independent of the pedalling frequency in order to satisfy the 95% confidence level criterion. Measurements for static-leg positions were sampled for 20 s at 2500 Hz. The random variability associated with phase-averaged data of each bin over 'N' crank revolutions is given by Eq. (2), where z_c=1.96 for a 95% confidence level:

$$\epsilon = \frac{z_c \sigma_{bin\#}}{\sqrt{N}}. \tag{2}$$

Time-averaged force measurements for static and dynamic pedalling conditions have also been obtained in the larger 1.4 MW 3/4 Open-Jet Wind Tunnel Facility at Monash University, which has a force measurement system installed. Open-jet

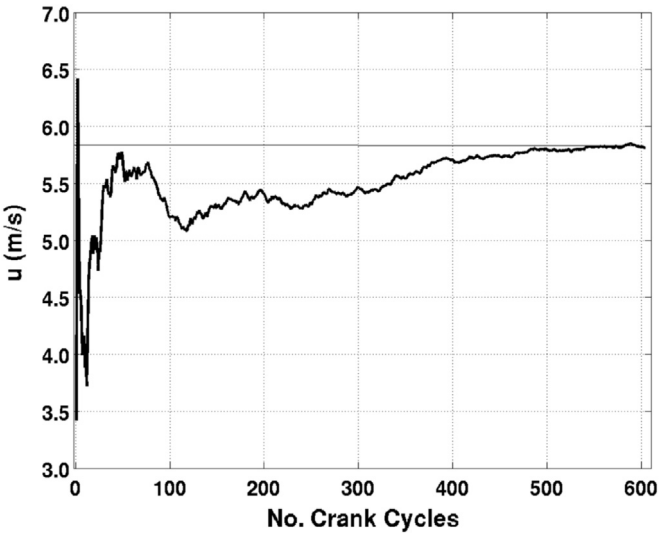

Fig. 3. Evolution of phase-averaged results of the streamwise velocity component as a function of number of crank cycles for a point in the wake and phase of the crank cycle where large velocity fluctuations are observed.

solid and wake blockage effects (< 5%) are small and so have been neglected. The force balance consists of four individual three-component piezoelectric force transducers (type-9067) positioned in a quadratic arrangement to provide measurements of the three force and corresponding moment components. The combined uncertainty associated with the force transducers and the National Instruments PXI-1050 (NI PXI-6284 card) data acquisition system is ±0.565 N over the force measurement range. Time-averaged force measurements are the result of averaging three separate tests sampled at 250 Hz for 40 s. The maximum variation in time-averaged forces for a particular static-leg position or cycling cadence was <0.6%.

3. Experimental results and discussion

In order to compare time-averaged quasi-steady and phase-averaged pedalling results at equivalent phases of the crank cycle, the corresponding crank angles assigned to the dynamic pedalling results have been corrected for the time taken for vortex structures to convect downstream to the measurement plane. The corresponding lag in the crank-angle phase, θ_{lag}, can be approximated by

$$\theta_{lag} = \frac{2\pi l_c f}{U_c}. \tag{3}$$

Here, l_c is the estimated streamwise distance between the velocity field measurement plane and the point on the body where vortices originate and U_c is the assumed constant convection velocity.

Although there is no one universal streamwise location that marks the origin of all longitudinal vortices, or indeed a single value of the convection velocity, both l_c and U_c have been taken as constant for the purpose of correcting the phase angle of phase-averaged flow fields. The streamwise spacing l_c=0.75 m has been taken as the distance between the hip-joint area, which marks the location of the separation node-saddle associated with the detachment of the upper hip vortex; see Crouch et al. (2014a) for details. This point serves as a representative location of the main flow structures of interest. Flow structures analysed in this study can be considered to primarily originate on the body from areas with l = 0.75 ± 0.1 m.

A number of methods have been developed to provide a reasonable approximation of the average velocity at which streamwise vortices, analysed in this investigation, convect downstream over the entire crank cycle. Techniques involving ensemble averaging of the velocity at the centre of vortices, as detailed by Zhou and Antonia (1992), place an equal weighting on each vortex that contributes to the estimated convection velocity. In this case, where longitudinal vortices spanning a range of scales are of interest, a method for estimating the convection velocity that places more emphasis on the convection velocity of the largest flow structures was adopted. This involved first identifying the boundaries of vortex structures in each of the phase-averaged velocity fields using the swirling strength vortex identification scheme of Zhou et al. (1999), then averaging the streamwise velocity component '$u_{c,Bin\#}$' of 'n' measurements which fall inside vortex boundaries,

$$U_{c,Bin\#} = \frac{1_c}{n}\sum_{i=1}^{n} u_{c,Bin\#,i}. \tag{4}$$

For the evenly spaced gridded data, a greater number of measurements are made within vortices of the largest size and hence a greater weighting is placed on their contribution to determining an 'overall' convection velocity. An average of $U_{c,Bin\#}$

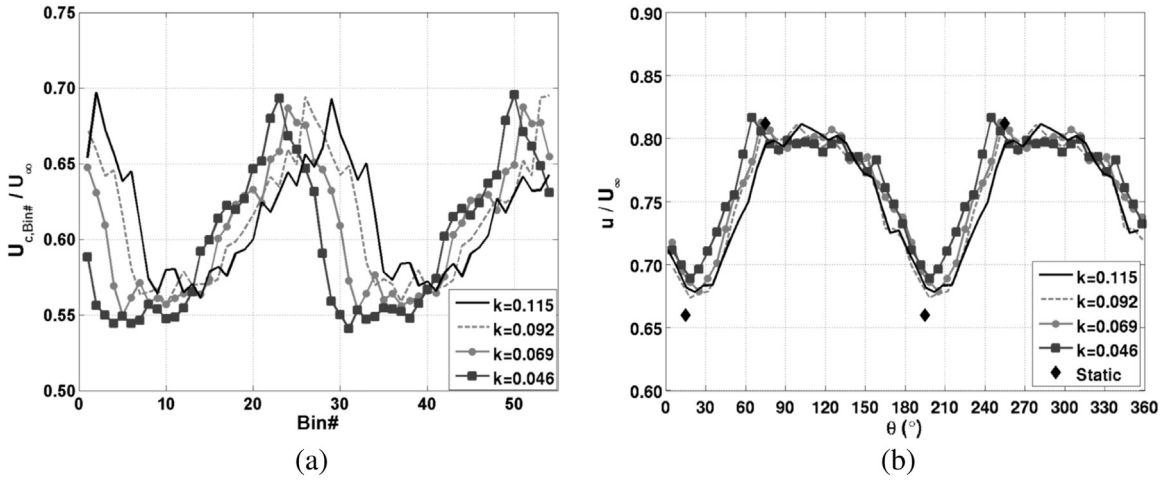

Fig. 4. (a) The estimated convection velocity of flow structures identified in phase-averaged velocity fields throughout the pedal stroke. (b) Time-averaged (static-legs) and phase corrected phase-averaged (dynamic-legs) results of the streamwise velocity component for a representative point in the upper wake.

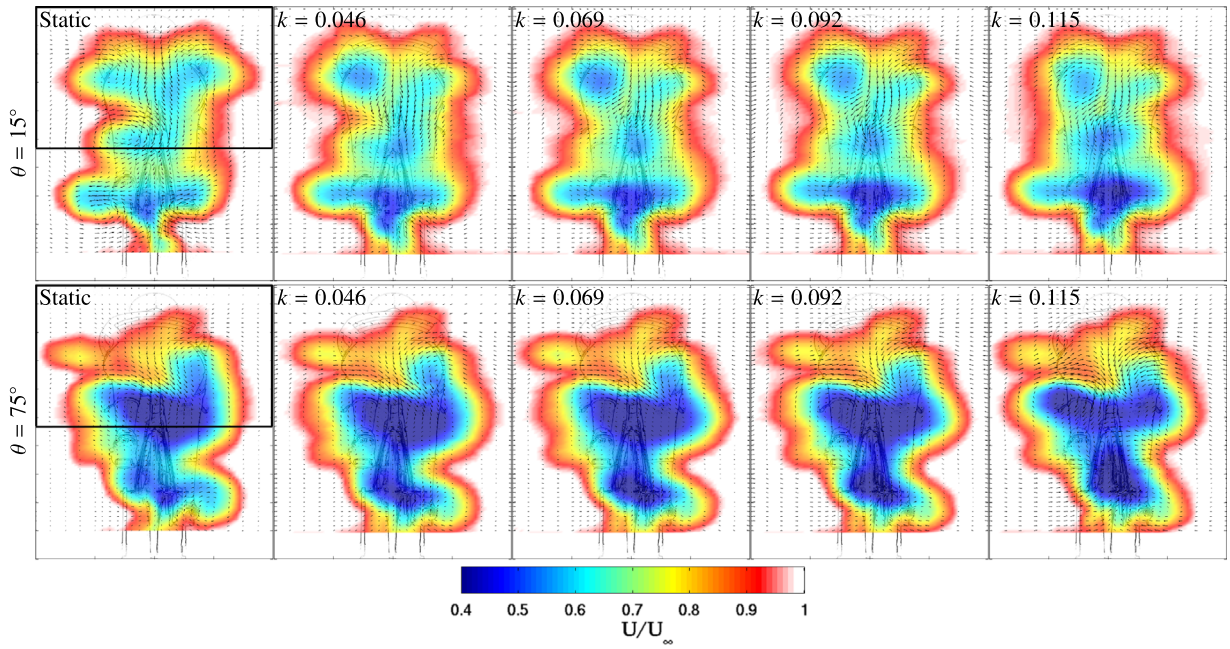

Fig. 5. Contours of time-averaged (static-legs) and phase-averaged (dynamic-legs, 40–100 RPM) streamwise velocity fields for symmetrical low (15°) and asymmetrical high drag (75°) phases of the crank cycle. The bold-box outlines the region of the wake analysed by Crouch et al. (2014a).

over all phase-averaged velocity fields (*Bin#*'s 1–54) was then taken as the convection velocity U_c representative of dominant wake flow structures passing through the measurement plane.

Fig. 4(a) shows the variation in $U_{c,Bin\#}$ for all the phase-averaged velocity fields and reduced pedalling frequencies. Apart from a clear phase offset (represented here by the Bin#), the variation in the estimated convection velocity throughout the crank cycle is very similar among all pedalling cases. Taking the average convection velocity across all the *Bin#*'s used to construct the phase-averaged velocity fields gives $U_c = 0.61U_\infty$, which varies <1.7% over all of reduced pedalling frequencies tested. Given this, a constant value of U_c has been assumed for all pedalling frequencies to correct for the phase-lag. (Note for the k=0.115 case this results in a phase-lag angle of θ_{lag}=46°).

Although the convection velocity varies in the range $0.55 \lesssim U_c \lesssim 0.70$ over the crank cycle, basing the phase shift on the average value results in a good collapse of data for different cadences. Fig. 4(b) shows for a representative point behind the hips (y=0, z = 1.0 m) phase-averaged results of the streamwise velocity component as a function of the phase-corrected crank angle for each cadence. Thus applying the phase-lag correction methodology outlined it can be seen that there is a good collapse of results over a large portion of the wake for the range of cadences examined. When taking into account the variation in $U_{c,Bin\#}$ for the different phases of the crank cycle and the uncertainty associated with l_c, the estimated maximum uncertainty in θ_{lag} is 18%. For the highest pedalling frequency this corresponds to $\theta_{lag} \pm 8°$, which is only slightly larger than the bin size used to obtain phase-averaged flow fields.

3.1. Wake structure of the pedalling cyclist

When pedalling phase-averaged measurements are corrected for the phase-lag there is good agreement between quasi-steady and phase-averaged flow fields. Fig. 5 compares contours of the out-of-plane streamwise velocity component between time-averaged (static-leg) and phase-averaged (k=0.046–0.115) flow fields. These are shown for phases of the crank cycle that are representative of the major symmetrical (θ=15°) and asymmetrical (θ=75°) flow regimes. For phases of the crank cycle about the 15° leg position the phase-averaged flow fields over the range of reduced pedalling frequencies compare well with the equivalent static 15° quasi-steady result. For this leg position, where the upper thighs are in near alignment (i.e., $\phi_{left} \approx \phi_{right}$), a near-symmetrical wake profile is observed about the centre plane for all cadences. Minor differences can be found in the lower region of the wake in-line with the crank where the leg motion occurs. In this region the magnitude of the streamwise velocity deficit progressively increases from the static to the highest pedalling frequency case. A slightly higher degree of symmetry is also observed in the flow for the static 15° leg position case, most notably in the upper wake above the hips ($z \geq 0.7$ m).

An even closer match is observed for the 75° leg position case as the cadence is changed. In the region of the wake $z \geq 0.7$ m, there is excellent agreement between quasi-steady and phase-averaged velocity fields. The size, magnitude and finer details in the asymmetry of the wake are consistent between all cases. There is also no significant change in the global wake structure described by Crouch et al. (2014a) for a slightly different model setup, suggesting that modifications made to

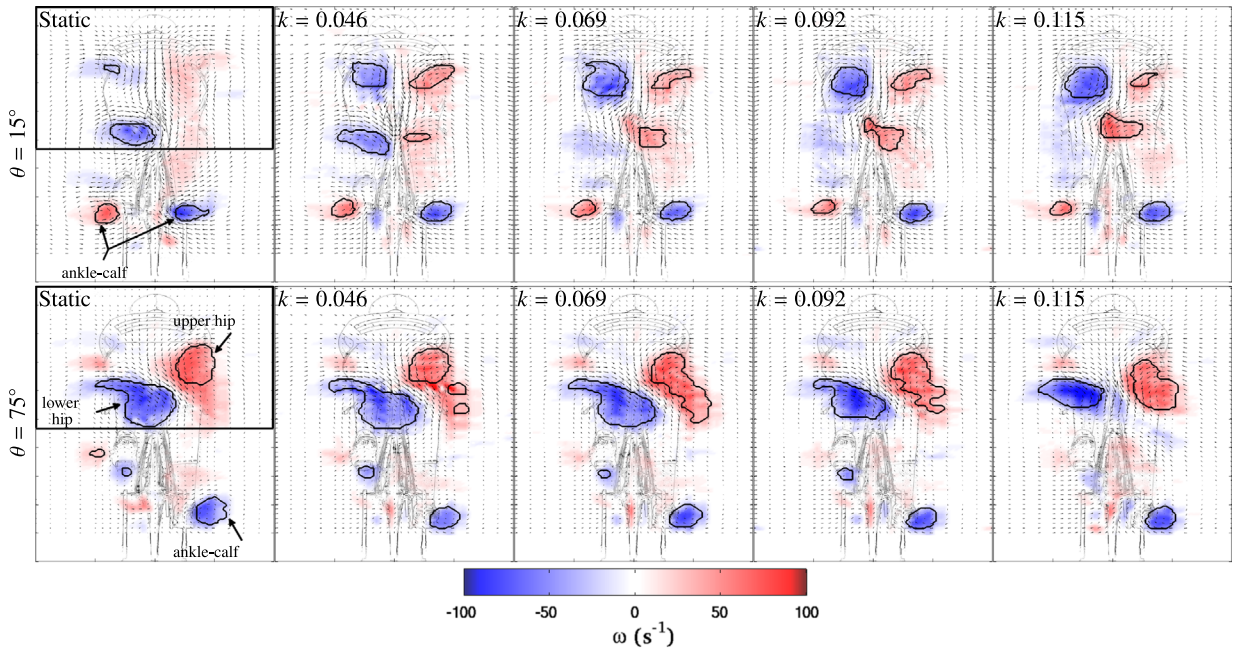

Fig. 6. Contours of time-averaged (static-legs) and phase-averaged (dynamic-legs 40–100 RPM) streamwise velocity fields for symmetrical low (15°) and asymmetrical high drag (75°) phases of the crank cycle. The bold-box outlines the region of the wake analysed by Crouch et al. (2014a).

the geometry and position of the model have had no significant effect on the flow topology.

Similar to the 15° leg position, an increase in the velocity deficit is found in the region of the wake where the leg motion occurs in-line with the crank for the reduced pedalling frequencies. Some of the variation can partially be explained by the phase-averaging process, where the velocity field is constructed based on a crank-cycle interval rather than a specific leg position. In particular this could be expected to influence the velocity field where there is a rapid change to the flow structure over a small rotation of the crank. This behaviour is observed when the flow transitions from the symmetric to the asymmetric flow regime. Due to the uncertainty associated with the phase-lag correction, it is not discernible whether a non-zero pedalling frequency results in a change in timing of switching between the asymmetrical and symmetrical flow regimes. Nevertheless, these differences are clearly relatively minor over the majority of the wake, showing broad consistency between the quasi-steady and phase-averaged cases for the two flow regimes.

Time-averaged and phase-averaged contours of the out-of-plane streamwise vorticity component in Fig. 6 show the large-scale flow structures of the upper and lower wake regions for the symmetrical and asymmetrical flow regimes. Streamwise vortices have been identified and are outlined using the swirling strength vortex identification scheme of Zhou et al. (1999). Once again, there is a closer match between quasi-steady and phase-averaged results for the asymmetric the flow regime case. The large-scale upper and lower hip vortex pair are closely matched in size, strength and orientation in the wake across all cases. These primary features of the wake, that originate from flow separating from the upper and lower hip regions, are responsible for the majority of the variation in drag over the crank cycle.

The phase-averaged fields for 15° the leg position show regions of streamwise vorticity with increased strength when compared with the equivalent quasi-steady result. Differences in the streamwise velocity deficit are also noticeable in these areas of the wake between static and moving-leg cases. Although they are much weaker, the evolved vortices associated with the asymmetrical flow regime that precedes the 15° leg position are evident in the phase-averaged flow fields, and are the strongest for the highest pedalling frequency case. A possible explanation lies in the uncertainty associated with the phase-averaging process and the phase-lag correction.

In addition to the large-scale vortices of the upper wake, smaller coherent vortical structures are also identified in the lower wake regions. The position of these vortices in the wake is well correlated with the movement and location of the lower leg/ankle-calf areas, and have been labelled in Fig. 6 accordingly. For both symmetrical and asymmetrical flow regimes there is very good agreement in the ankle-calf vortices across quasi-steady and phase-averaged flow fields. For static and dynamic pedalling fields corresponding to the 15° leg position, ankle-calf vortices of similar size and opposite sign are observed for both left and right lower legs. For the asymmetric 75° leg position, all cases show only a single ankle-calf vortex, originating from the lower leg, which is in an extended position (right-hand side for θ=75° shown).

A more detailed picture of how the upper and lower vortical structures evolve over the dynamic pedal stroke is shown in Fig. 7. This figure shows phase-averaged contours of the streamwise vorticity field for selected phase angles in the first half of the crank cycle for the highest pedalling frequency (k=0.115). Starting at the 15° phase angle and working across and down to the 195° position, it can be seen that the transition from the symmetrical to the asymmetrical flow regime is at

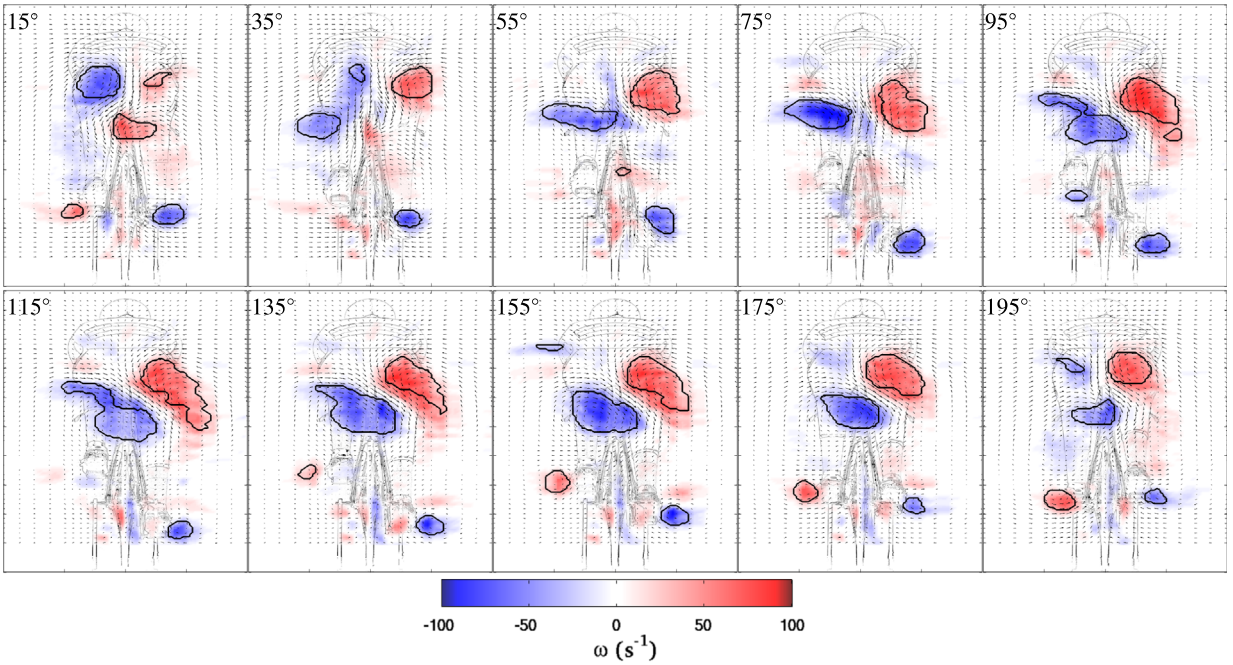

Fig. 7. Contours of phase-averaged streamwise vorticity fields in the first half of the crank cycle for a reduced cycling frequency of $k=0.115$ (100 RPM).

approximately $\theta=15°$. As the left leg rises and the right leg recedes from the chest in this half of the cycle, the upper (right) and lower (left) hip vortices are formed. These structures grow in strength and a decrease in the degree of flow symmetry is observed as the left leg meets the chest at $\theta=75°$. The ankle-calf vortices of the lower wake can be seen to follow with the position of the lower leg from where they originate throughout the stroke. Both left and right ankle-calf vortices are present in the measurement plane at $\approx 60°$ prior to and $\approx 10°$ following the symmetrical leg position, where the upper thighs are aligned $\phi_{left} = \phi_{right}$.

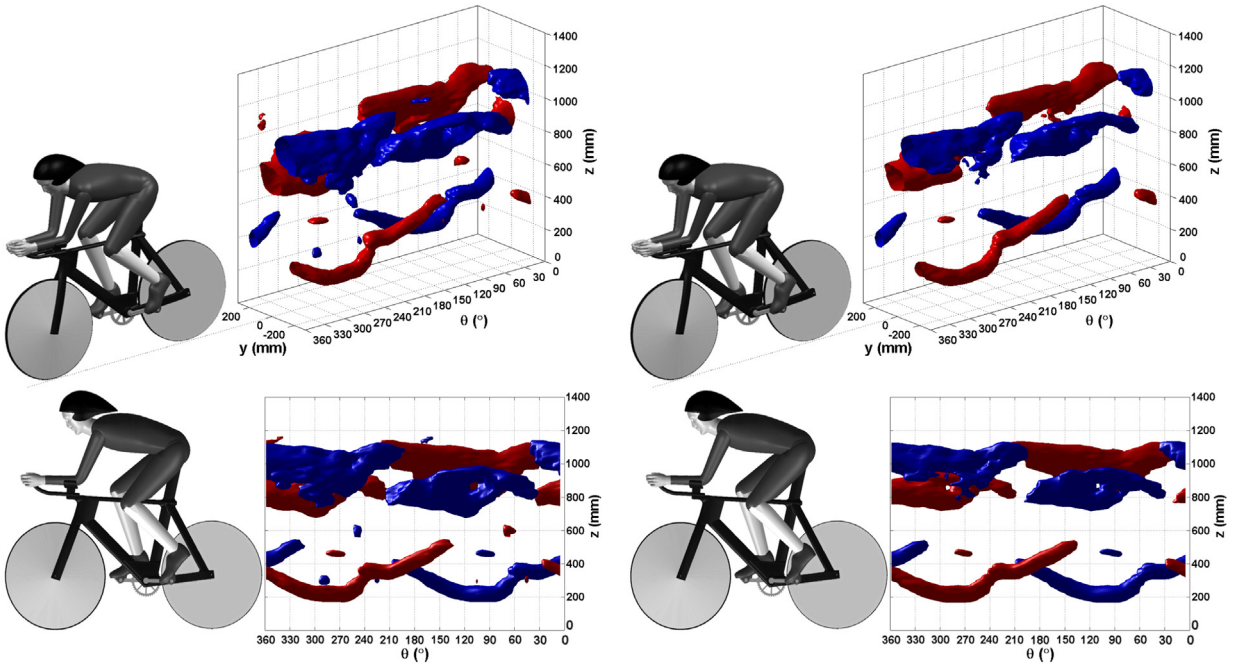

Fig. 8. (a) Vortex structures visualised from different perspectives using surfaces of the swirling strength criterion throughout a complete crank cycle for the highest pedalling frequency case (100 RPM). (b) Isosurfaces where streamwise vortices are common among all reduced pedalling frequencies.

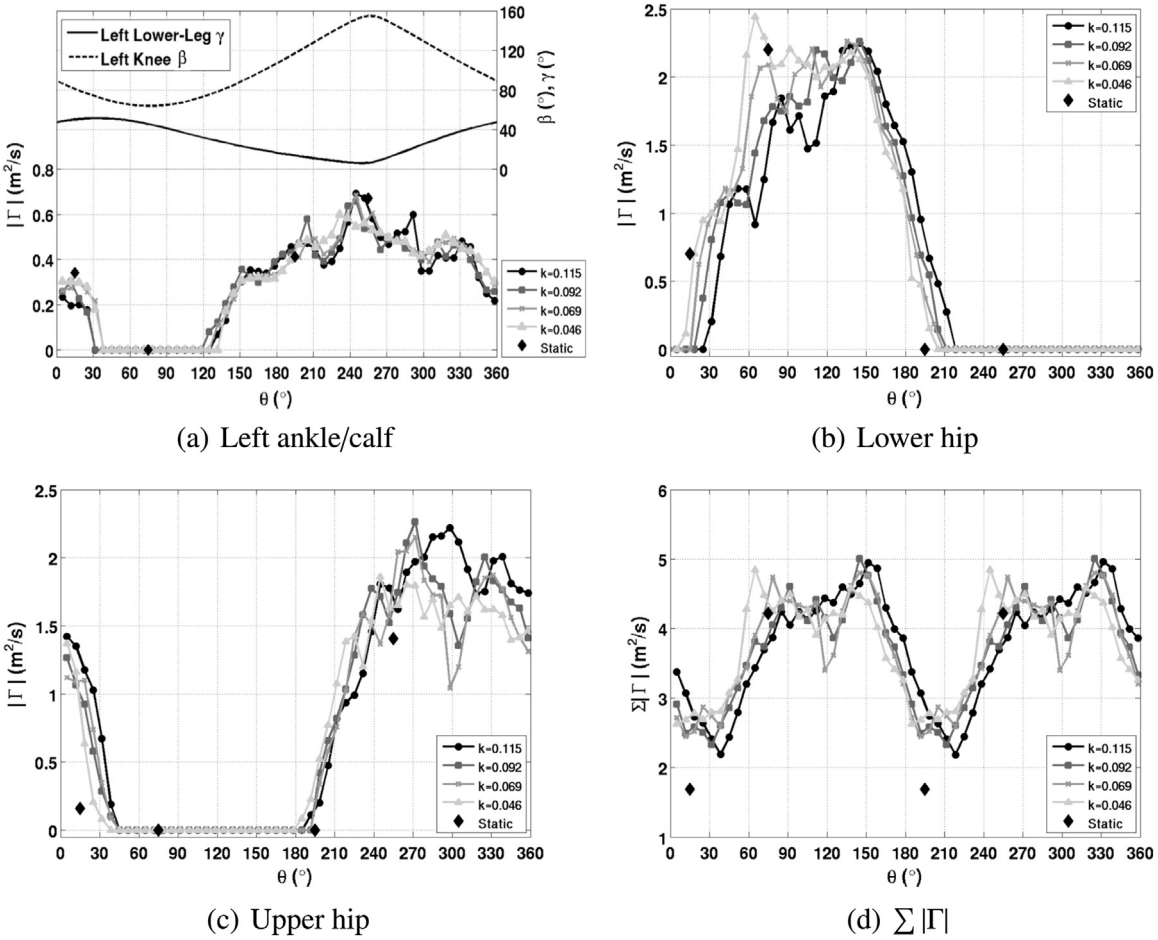

Fig. 9. Circulation (absolute value) of (a) left ankle-calf vortex, (b) left lower hip vortex, (c) left upper hip vortex and (d) total wake circulation, $\sum(|\Gamma_{ankle/calf}| + |\Gamma_{lowerhip}| + |\Gamma_{upperhip}|)$.

For the highest reduced pedalling frequency case ($k=0.115$) Fig. 8(a) shows a three-dimensional representation of the upper and lower wake vortices depicted from two different perspectives over the complete crank cycle. The isosurfaces of swirling strength depict the streamwise vortex boundaries and clearly show the downstream development of the upper hip, lower hip and ankle-calf vortices over the crank cycle. To construct these images, it is assumed that these vortices convect downstream at the mean convection velocity derived previously. The 'flipping' of the upper and lower hip vortices from left- to right-hand sides, as well as the vertical displacement of the ankle-calf vortices, are evident throughout the 360° dynamic pedal stroke. When similar visualisations of these flow structures are made for the other pedalling frequencies ($k=0$, 0.046, 0.069, 0.092), near identical isosurface patterns are observed. This is demonstrated in Fig. 8(b), which shows *common* streamwise vortical structures over all reduced pedalling frequencies investigated. Effectively, if similar isosurfaces, as drawn in Fig. 8(a), are overlaid for all of the pedalling cases, Fig. 8(b) shows vortical regions that are the volume intersection of the set. The fact that Figs. 8(b) and (a) are nearly identical, apart from the smallest-scale features, demonstrates that the same wake flow structures are present and are very similar across all pedalling frequencies investigated and throughout the same phases of the crank cycle.

3.2. Effect of cadence on vortex strength

Although the global structure of the wake is maintained, some variations in the strength of the primary vortices are evident between the various pedalling cases. Surface integrals of the streamwise vorticity over these identifiable structures were calculated to determine the circulation of the ankle-calf, lower hip and upper hip vortices: $\Gamma = \iint_A \omega_x da$. The magnitudes of these circulations as a function of crank angle are shown in Figs. 9(a)–(c) for all reduced frequencies. Fig. 9(a) shows the strength of the left ankle-calf vortex as a function of crank angle. Also shown are the left lower leg and knee angles, which are drawn with respect to the right-hand axis as a function of crank angle. Little variation in the strength of the ankle-calf vortex exists throughout the entire pedal stroke between different reduced frequencies. As the left-lower leg angle reaches a maximum (its most inclined position with respect to U_∞) and the knee angle begins to close, the left-ankle-

calf vortex is not identified in the measurement plane. As the left knee angle reaches a minimum and begins to open, at approximately 120° crank angle, the ankle-calf vortex reappears in the plane and increases in strength until ≈255° (high-drag leg position). This crank angle corresponds to when the left knee is at its most open position and the lower leg axis is approximately perpendicular to the freestream. Figs. 9(b) and (c) show the strength of the left lower hip and upper hip vortices, respectively. The mean magnitude and variation in the strength among these vortices throughout the pedal stroke shows good agreement with the quasi-steady investigations. In general the strength of these vortices increase rapidly from the low drag leg positions to higher drag leg positions where they are strongest. The most noticeable influence of the pedalling cadence on the strength of these vortices is found in the lower hip vortex. For increasing cadence, the circulation of the lower hip vortex is shifted to higher crank phase, notably greater than the uncertainty associated with the phase lag $\approx \pm 8°$. There is also a consistent reduction in circulation around the high drag 60–90° leg positions. Comparing total circulation levels, defined as $\sum (|\Gamma_{ankle/calf}| + |\Gamma_{lowerhip}| + |\Gamma_{upperhip}|)$, over the different pedalling frequencies, Fig. 9(d) shows that overall there is a discernible shift in wake circulation to higher phases of the crank cycle with increasing cadence. The total wake circulation also peaks earlier in each half of the crank cycle under quasi-steady conditions ($\approx 75°$) and is shifted towards high crank angles ($\approx 150°$) as the cadence is increased. Lower wake circulation levels are also observed for the static 15° leg position compared to the moving-leg cases. This is due to circulation levels associated with the upper hip vortices, which are present in all moving-leg cases but not the static 15° leg position. Once again, it is not discernible whether this is a result of the phase-averaging process, the uncertainty associated with the phase-lag correction or the leg-motion is influencing the wake dynamics for this particular leg position.

As the formation and strength of the wake vortices is dependent on leg position it is important to consider how a fixed ankle joint may influence these structures throughout the pedal stroke. To constrain and simplify the motion of the legs the ankle joint of the mannequin is fixed ($\Omega = 112.5°$). To assess the impact that this may be having on wake vortices, the dynamics of the upper and lower legs have been modelled for the geometry of the mannequins legs with a varying ankle joint. Although the motion of the ankle joint will vary from athlete to athlete, typically when the crank is at top dead centre the ankle joint angle is reduced and when the crank is at the bottom of the stroke the angle joint opens up. Fig. 10 (a) reproduces results from Ericson et al. (1986), showing the ankle angle Ω as a function of the crank angle. A sinusoidal fit has been applied to this data and has been used to approximate the motion of the ankle joint throughout the pedal stroke. Fig. 10(b) shows the extent to which the ankle joint influences the hip and lower leg angles of the mannequin throughout a full rotation of the crank.

For a common pedal stroke, where the variation in the ankle joint is typically <30°, it is unlikely that the addition of a mobile ankle joint will result in a complete reorganisation of the wake flow structure. Varying the ankle joint does not have a significant effect on the lower leg inclination angle and motion throughout the pedal stroke. The largest impact of the ankle joint is on the variation in the hip angle throughout the pedal stroke. Crouch et al. (2014a,b) showed that the circulation of the rear hip vortices was strongly correlated with the hip angle. The ankle joint reduces the range of motion of the upper leg. As a result it is expected that the circulation of the hip vortices will be slightly reduced with the addition of a flexible ankle joint. The extent to which the strength of the wake vortices may be influenced or if there are additional yet to be discovered flow mechanisms and interactions within the foot/ankle area requires further investigation.

3.3. Cadence and aerodynamic resistance

When optimising cycling aerodynamics the main objective is to minimise the aerodynamic drag across the entire pedal

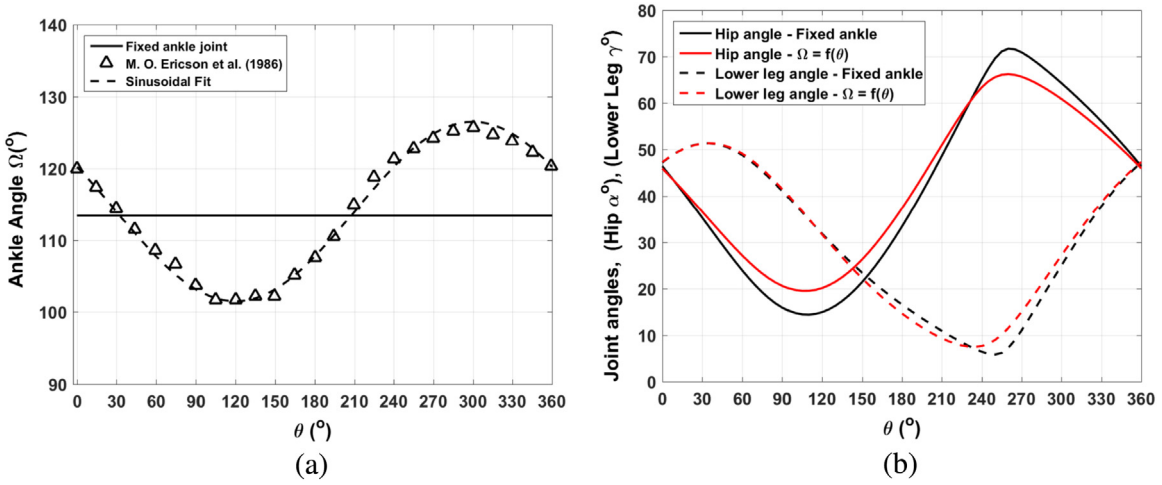

Fig. 10. (a) Ankle joint angle as a function of crank angle, from Ericson et al. (1986). (b) Left leg joint angles as a function of the crank angle for the current fixed joint set-up and a set-up where the ankle joint moves throughout the pedal stroke.

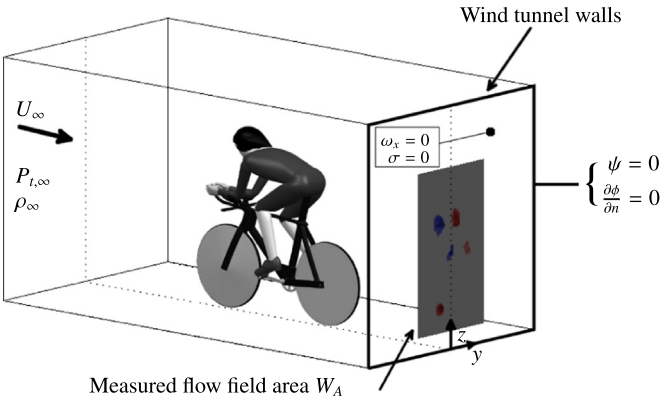

Fig. 11. Control volume used to calculate wake integral C_DA values.

stroke, or equivalently to minimise the time-averaged aerodynamic drag force. If there is little difference in the wakes generated by quasi-steady and pedalling cyclists, one might expect that there is little to gain, in terms of reducing aerodynamic drag, by trying to optimise cycling cadence. To investigate this hypothesis aerodynamic forces are analysed as a function of crank angle for the reduced pedalling frequencies tested for the moving-leg model.

From the measured phased-averaged velocity and pressure fields obtained in the downstream measurement plane, estimates of the aerodynamic drag force have been made based on the wake integral methods of Maskell (1973) and Betz (1925). The wake integral method allows the aerodynamic drag to be approximated through integrating the momentum equation over a control volume surrounding the model. Good agreement has been found between direct force balance measurements and this wake integral approximation for a wide range of flows. For example, studies using multi-hole pressure probes (similar to those used in this study) to survey the vortical wakes of finite high-lift airfoils (Brune, 1994; Kusunose, 1997) as well as the separated wakes of bluff-body geometries such as road vehicles (Wu, 1982; Hackett and Sugavanam, 1984) have provided estimates of aerodynamic forces acting on these bodies that are in agreement with more direct methods. Detailed descriptions of the derivation of the wake integral approach are provided by these studies and thus only a brief summary of the approach used to determine phase-averaged estimates of drag will be given here.

From a control volume that surrounds the cyclist model, which is pictured in Fig. 11, the total drag area can be expressed as the sum of two terms integrated over the viscous wake area 'W_A' and the wind tunnel cross-sectional area 'A':

$$C_DA = \iint_{W_A} \frac{(P_{t\infty} - P_t)}{\frac{1}{2}\rho_\infty U_\infty^2} + \frac{1}{U_\infty^2}(u^* - u)(u^* + u - 2[U_\infty + u_b])\,\mathrm{d}y\mathrm{d}z + \iint_A \left(\frac{v}{U_\infty}\right)^2 + \left(\frac{w}{U_\infty}\right)^2 \mathrm{d}y\mathrm{d}z, \tag{5}$$

where U_∞, ρ_∞ and $P_{t\infty}$ are the reference free-stream velocity, density and total pressure, respectively, and u^* and u_b are known as the Betz artificial wake axial velocity and Maskell's wake blockage correction, respectively. With u^* defined as:

$$u^* = \left(u^2 + \frac{1}{\rho_\infty}[P_{t\infty} - P_t]\right)^{1/2}, \tag{6}$$

the blockage velocity is calculated from:

$$u_b = \frac{1}{2A}\iint_{W_A} (u^* - u)\,\mathrm{d}y\mathrm{d}z. \tag{7}$$

The first term in Eq. (5) is commonly referred to as the profile drag D_p and the second the induced drag D_i. To limit the wake integrals to the viscous part of the wake, Maskell introduced the following approximation to the induced drag term:

$$D_i \approx \frac{\rho}{2}\iint_{W_A} \omega_x\psi\,\mathrm{d}y\mathrm{d}z - \frac{\rho}{2}\iint_A \sigma\phi\,\mathrm{d}y\mathrm{d}z, \tag{8}$$

where σ is the cross-flow divergence $\sigma = \frac{\partial v}{\partial y} + \frac{\partial w}{\partial z}$ (source term), and ψ and ϕ represent the in-plane scalar stream and velocity potential functions, respectively. As the velocity potential integrand is often negligible outside the viscous wake region, Eq. (8) can be further simplified to:

$$D_i \approx \frac{\rho}{2}\iint_{W_A} (\omega_x\psi - \sigma\phi)\,\mathrm{d}y\mathrm{d}z. \tag{9}$$

In evaluating the induced-drag term, the scalar stream and velocity potential functions are obtained from a solution of the Laplace and Poisson equations:

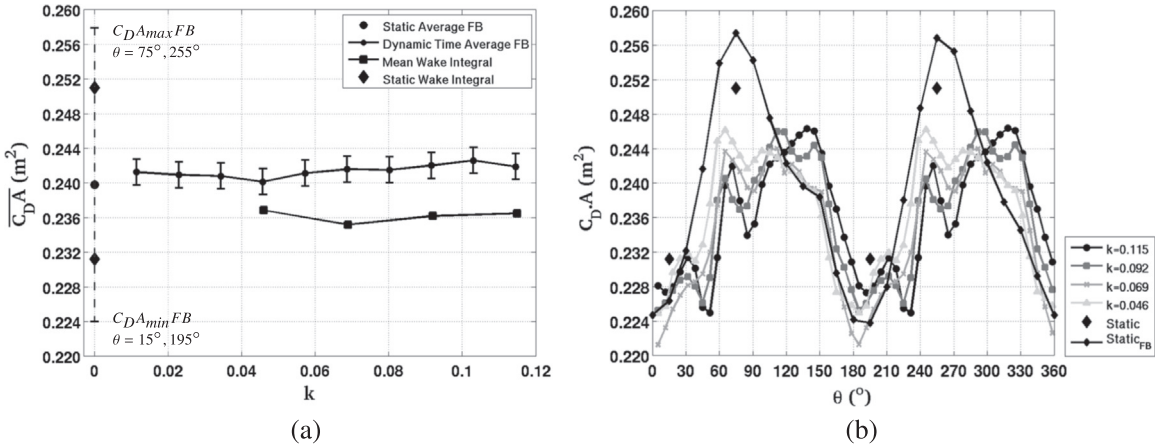

Fig. 12. (a) Time-averaged force balance measurements and mean pedal-stroke wake integral $\overline{C_DA}$ values for various reduced pedalling frequencies. The maximum and minimum force balance measurements of static-leg positions are represented by the upper and lower error bar bounds. (b) Phase-averaged C_DA results compared with quasi-static force balance measurements as a function of crank angle.

$$\frac{\partial^2\psi}{\partial y^2} + \frac{\partial^2\psi}{\partial z^2} = \begin{cases} -\omega_x, & \text{inside wake} \\ 0, & \text{outside wake} \end{cases}, \tag{10}$$

$$\frac{\partial^2\phi}{\partial y^2} + \frac{\partial^2\phi}{\partial z^2} = \begin{cases} \sigma, & \text{inside wake} \\ 0, & \text{outside wake} \end{cases}, \tag{11}$$

subject to the boundary condition $\psi = 0$ at the wind tunnel walls (noting that the boundary is a streamline), and $\frac{\partial\phi}{\partial n} = 0$ (no flow through the wind tunnel walls), with n being the wall-normal direction.

Fig. 12(a) compares drag area estimates obtained from the wake integral analysis that have been averaged over the crank cycle (integral average) with time-averaged force balance measurements, both as a function of reduced pedalling frequency. The figure also depicts the integral average of static-leg force-balance results measured at 15° increments in leg position around a complete crank cycle. From an average point of view, $\overline{C_DA}$ results are in very good agreement with both direct force measurements and wake integral predictions for all reduced frequencies. Both time-averaged force-balance measurements and wake integral C_DA approximations show that there is no significant change to the average aerodynamic drag force around the crank cycle as the pedalling cadence is increased from quasi-steady to elite-level values. Across all of the pedalling frequencies tested, the variation in the force is within the experimental uncertainty. Fig. 12(b) shows that direct force-balance measurements of quasi-static leg positions varied by ≈15% through the crank cycle. The aerodynamic drag peaks at the 75° and 255° static leg positions, and reaches a minimum between 0–15° and 180–195° positions from these measurements. At the low-/high-drag static leg positions there is an ≈2% variation in C_DA between the force balance measurements and those evaluated using the wake integral method. The range of C_DA values between the high- and low-drag leg positions is also smaller for the wake integral results (9% compared with ≈ 15%). The differences between methods are not unreasonable, given that the independent sets of results have been obtained in separate wind-tunnel environments and assumed flow symmetry (for opposing crank angles) has been enforced on the velocity and pressure fields used to evaluate the wake integrals. The uncertainty due to the variability of phased-averaged flow field quantities measured with the multi-hole probe used in the determination of C_DA from Eq. (5) is estimated to be <0.5%.

Although pedal-stroke averaged C_DA results show little dependence on cadence, focussing on drag area values over specific phases of the crank cycle shows that there is a distinct departure from quasi-steady results as pedalling cadence is increased. In general, these differences are consistent with the variation in the strength of the large-scale vortices that was observed for the different pedalling frequencies. These are as follows:

1. Phased-averaged force results are shifted towards larger crank angles with increasing cadence. This appears as a phase offset of $\Delta\theta \approx 30°$.
2. A redistribution of the aerodynamic drag force in each half of the crank cycle. This is observed as reduction in the aerodynamic drag about the high-drag quasi-steady leg positions, and a shift in the peak drag towards later stages of the crank cycle as the reduced pedalling frequency increases. (This effect is larger than the above mentioned phase shift).

Although other differences are clearly evident, these constitute the largest and most consistent differences between the experimental data sets. These results suggest that a circular pedal stroke optimised for aerodynamics performance will involve varying the pedalling angular velocity throughout the crank cycle.

3.4. A crude moving-leg aerodynamic force model

Insight into the dominant mechanisms leading to variations in C_DA with increasing cadence is gained by considering a simple quasi-steady model of the aerodynamic drag acting on the upper legs, lower legs and crank-arm that accounts for changes in local leg/crank velocity when these bodies are set in motion. The model is based on the independence principal, which provides an estimate of the aerodynamic drag force acting on a circular cylinder orientated at an angle (yawed) to the freestream (Schlichting and Gersten, 2000). The independence principal is also known as the cosine-law as the aerodynamic drag force F_D is derived from the component of the freestream velocity that acts normal to the cylinder axis $U_{\infty\perp}$. The drag force in effect is likened to the force experienced by a cylinder in a pure cross flow via $F_D = 1/2\rho_\infty U_{\infty\perp}^2 C_D D$, where D is the cylinder diameter. This reasoning has been applied to simulate the aerodynamic drag force acting on the legs and crank-arm throughout the stages of the pedal stroke, where the legs are modelled as simple tapered cylindrical sections and the crank-arm as a cylinder.

This is a rather crude model that is unable to capture the details of the flow physics that determine the magnitude of the aerodynamic drag force acting on each leg member. For one, end effects and aerodynamic interactions between the legs, body and the bicycle frame are not modelled. Flow interactions exist between various components of the bicycle/rider system that with influence the magnitude of the aerodynamic forces. Aerodynamic forces acting on the upper-leg, lower-leg and the crank arm are simulated as if these components are in isolation of one another and the rest of the bicycle/rider system. In reality the legs are in the turbulent wake regions of upstream body and bicycle components and exhibit strong flow interactions between upper/lower leg sections, the bicycle frame and other surrounding body components. The model also does not take into account aerodynamic forces acting on other parts of the body that may also contribute to the measured variations in C_DA with cycling cadence. The aerodynamic performance of the wheels under rotation is not considered, which has been shown to be important for spoke wheels such as those used in this study (Karabelas and Markatos, 2012). Despite all these simplifying assumptions, it does allow focus on a single aspect of the leg motion: the change in local velocity that the legs experience under varying cycling cadence and a semi-quantitative assessment of the impact that cycling cadence may have on changes in the aerodynamic drag force over the course of the pedal stroke.

Fig. 13 shows a pictorial representation of the model and defines the major components required for simulating the aerodynamic drag acting on the moving legs using the independence principal. The leg motion is modelled by a four-bar crank rocker mechanism consisting of the crank-arm *AB* and rigid lines connecting the foot pivot point and knee joint *BC* and knee and hip-joint *CD*. From the dimensions provided in Table 1, the position and orientation of the upper and lower legs can be defined as a function of the crank angle. With the orientation of the legs known, the component of the freestream velocity acting normal to the leg axes can be found. For a given pedalling rate $\dot{\theta}$, the rotational rate of the upper leg about the hip joint $\dot{\alpha}$, and the rotational $\dot{\gamma}$ and translational velocity components $(U_{x'}, V_{y'})$ of the lower leg with respect to the knee joint (x', y') coordinate system can be evaluated. In simulating the aerodynamic drag force, rotational and translational velocity components in the freestream direction (x') that act normal to the leg axes are added to the quasi-steady force model. The general equation for the drag force per unit leg/crank length F_D' with the addition of rotational and translation components:

$$F_D' = \tfrac{1}{2}\rho_\infty C_D D[U_{\infty\perp} + U_{x',\perp} + (\omega_o Q)_{x',\perp}]^2, \tag{12}$$

can be integrated over the length of each upper leg $(l = 0 \rightarrow L)$, lower leg $(s = 0 \rightarrow S)$ and crank arm $(h = 0 \rightarrow H)$, and

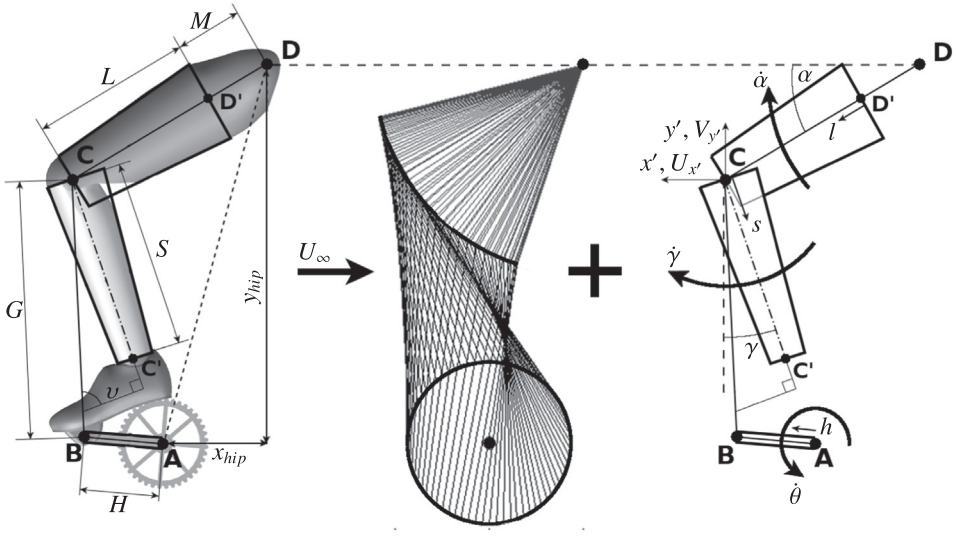

Fig. 13. Pictorial representation of the moving leg force model.

Table 1
Full-scale model leg dimensions.

Name	Symbol	Length (mm)	Name	Symbol/Location	Length (mm)
Crank-arm	AB	$H=175$	Hip location (x)	x_{hip}	200
Foot-pivot to knee joint	BC	$G=558$	Hip location (y)	y_{hip}	806
Lower leg	CC'	$S=410$	Crank diameter	A	12
Upper leg	$D'C$	$L=350$	Upper leg diameter	D'	172
Hip	DD'	$M=100$	Knee diameter	C	117
Lower leg offset angle	υ	73.5°	Lower leg diameter	C'	62

summed for left and right sides of the body to evaluate the total drag area C_DA_{Total} of the leg-crank system as a function of the crank angle and rotation rate:

$$C_DA_{Total}(\theta,\dot{\theta}) = \frac{1}{\frac{1}{2}\rho_\infty U_\infty^2}\left(\int_0^H F'_{D_{AB}}\,dh + \int_0^S F'_{D_{CC'}}\,ds + \int_0^L F'_{D_{D'C}}\,dl\right)_{left+right}. \tag{13}$$

Here, ω_o and Q represent the leg/crank angular rotation rate and distance along the member where F'_D is evaluated (referenced to where ω_o is measured). Note that subscripts AB, CC', $D'C$ represent the crank-arm, lower leg and upper leg members, respectively, and x' and $\perp$ indicate leg motion velocity components acting in the x' direction and perpendicular to the member axis, respectively.

3.5. Applications of the moving-leg model

The moving-leg force model has been applied to the wind tunnel cyclist leg geometry for a number of idealised scenarios. Fig. 14(a) shows the total left and right leg drag area calculated using Eq. (13) for the simplest case where the local leg drag coefficient is taken as a constant $C_D=1.1$ for various pedalling frequencies (0–100 RPM) at a freestream velocity of 16 m/s. Despite the idealised scenario of assuming a drag coefficient of 1.1, the simple model predicts the average phase shift ($\approx 30°$) that is observed between the experimental quasi-steady and phase-averaged force results for the largest pedalling frequency. These findings were also observed when the local leg drag coefficient $C_{D_{local}}$ was based on the local leg section Reynolds number Re_{local}. The largest influence of simulated drag area values as a function of the Re_{local} was not to the average phase shift but to mean crank drag area results and the peak-to-peak variation in the drag area between the high and low drag leg positions. Depending on the $C_{D_{local}} = f(Re_{local})$ function employed, the variation in the summed drag area of both legs around a full pedal stroke was of the order of $\approx$ 5–30%. Although accurate predictions of absolute drag results are unable to be obtained, trends observed between static and pedalling cases are consistent for the various scenarios tested. This model can at least partially account for the measured phase shift in force, going beyond explaining these variations simply due to the uncertainty associated with the wake integral technique and the inadequacies in determining the phase-lag correction.

Further similarities between experimental and the simulated forces are found when the average aerodynamic drag force over the entire pedal stroke is considered. Mean simulated drag area values for cases where the local leg drag coefficient has been assumed constant and as a function of Re_{local} are of the same order predicted by higher-order computational fluid solver models, which estimate the contribution from the legs to the total aerodynamic resistance as $\approx$ 30–40% (Defraeye

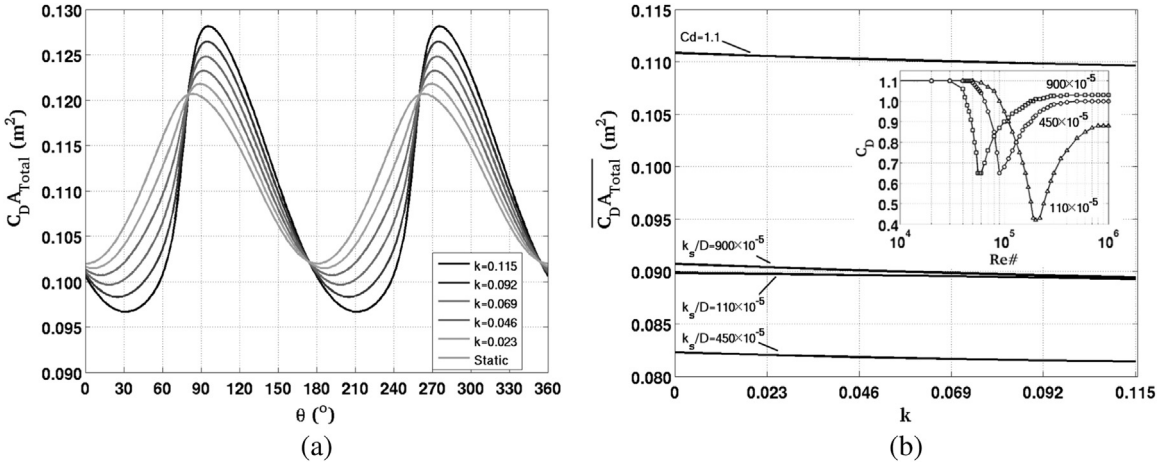

Fig. 14. (a) Simulated left and right leg C_DA for stationary and pedalling conditions as a function of the crank angle for $C_D=1.1$. (b) Simulated leg C_DA values averaged over the pedal stroke calculated for various $C_D = f(Re_\perp, k_s/D)$.

et al., 2011; Griffith et al., 2014). Similar to the time averaged force balance results, modelled aerodynamic drag forces that are averaged over the entire pedal stroke show very little dependence on the pedalling frequency. Fig. 14(b) shows the simulated mean pedal-stroke drag area as a function of the reduced pedalling frequency. For the simplest case where C_D is constant, the drag area varies <0.5% over the range of reduced frequencies of this study.

The model has also been used to test if local changes in the leg Reynolds number, which cover the critical-transition flow regime ($6 \times 10^4 \lesssim Re \lesssim 2 \times 10^5$), are likely to impact the mean pedal-stroke drag area as the leg speed is increased. One could envisage a scenario where speeding up the rotational rate of the legs around the crank (increasing the reduced pedalling frequency 'k') could induce, prolong or shift where drag crisis occurs on the leg and around phases of the pedal stroke that would not have otherwise occurred at lower cycling cadences, resulting in a change to the time-averaged aerodynamic force. Fig. 14(b) also shows $\overline{C_D A}$ results where the local leg drag coefficient has not been assumed to be constant, for three cases that are representative of legs with surface texture grain heights of 0.1–1.5 mm (dependent on the position along the legs). The drag coefficient functions $C_D = f(Re_\perp, k_s/D)$, where k_s/D is the roughness parameter, used to simulate the influence of leg surface texture are based on the experimental results of Achenbach (1971) for circular cylinders $k_s/D = 110 \times 10^{-5}$, 450×10^{-5}, 900×10^{-5} (smooth to rough). Although the roughness parameters selected are somewhat representative of bare skin, textured fabric or hairs on the legs, the main reason for selecting these values is that they cover the range where drag crisis occurs over the Reynolds numbers relevant to the upper and lower legs. If local changes in Re of the upper and lower legs, induced by varying pedalling cadence, can generate a change in the time-averaged aerodynamic drag this will most likely be observed for scenarios where the function $C_D = f(Re_\perp, k_s/D)$ of the legs has a large gradient. Again, when this added complexity is included, the simulated results suggest that it is unlikely that further gains in aerodynamic performance are to be had through optimising cadence speed. The local change in Re induced by the leg motion is unlikely to have a significant influence on the mean pedal-stroke aerodynamic drag force.

A more comprehensive understanding of why variations in C_DA occur as cadence is increased is gained by considering the simulated aerodynamic drag force acting on each leg member. As expected, when forces on the legs are analysed on a single side of the body (left or right), changes in C_DA from stationary conditions depend upon how fast the leg is translating/rotating upwind or downwind. The degree to which the motion of the legs results in a departure away from stationary leg results is dependant on the phase of the crank cycle.

For the upper legs this is demonstrated in Fig. 15, which shows the simulated aerodynamic drag force acting on each left and right upper leg around the crank cycle. An explanation for how cadence can influence forces on the upper legs is revealed by considering the aerodynamic drag force at a phase in the crank cycle where the left leg hip angle is at a minimum $\theta \approx 110°$ (close to the chest). At this point in the cycle, where the rotational speed of the left leg $\dot{\alpha}_{left} \simeq 0$, there is no change to the simulated left upper leg drag area between static and pedalling cases. As $\frac{d\alpha}{d\theta}$ and α are small in this crank-angle range for the left-leg ($50° < \theta < 170°$), an increase in the pedalling cadence to elite-level rates will not result in any significant change from the stationary quasi-steady conditions.

In contrast, the opposite (right) leg is in a crank-cycle range where $\frac{d\alpha}{d\theta}$ and α are relatively large. As a result the rotational velocity $\dot{\alpha}_{right}$ of the right upper leg at this phase will act to increase the aerodynamic drag force experienced by the leg and will continue to increase with the pedalling rate $\dot{\theta}$. When the C_DAs of both left and right legs are added together, it is this asymmetry in the right/left upper leg motion that primarily contributes to the phase shift in the force signal as the cadence is increased. A measure of this asymmetry is given by $([\dot{\alpha}(l+M)]_{x',\perp,left} + [\dot{\alpha}(l+M)]_{x',\perp,right})$: the addition of the effective

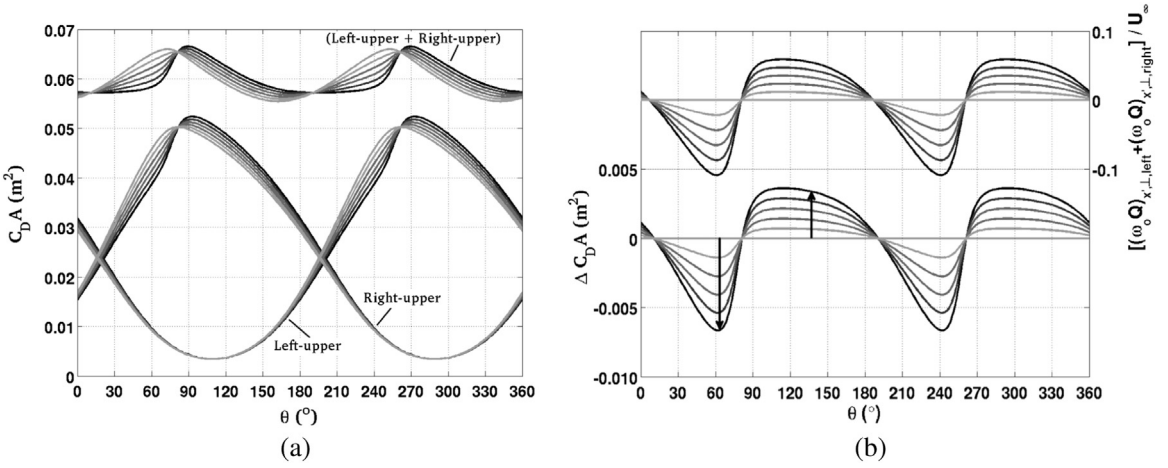

Fig. 15. (a) Aerodynamic drag area simulated on the upper leg for various reduced pedalling frequencies. (Note 0.01 m^2 has been added (left-upper+right-upper) to simulated C_DA results for clarity). (b) Lines plotted with respect to the left-hand axis show the variation in $C_DA_{upperleg}$ from static upper leg conditions. The asymmetry in the rotational motion of the upper left/right legs, defined by $([\dot{\alpha}(L+M)]_{x',\perp,left} + [\dot{\alpha}(L+M)]_{x',\perp,right})$, is plotted with respect the right-hand axis. (Note that the colours of the lines have been graduated from light to dark to mark simulated C_DA results for increasing reduced pedalling frequencies, where $k = 0$, 0.023, 0.046, 0.069, 0.092, 0.115.)

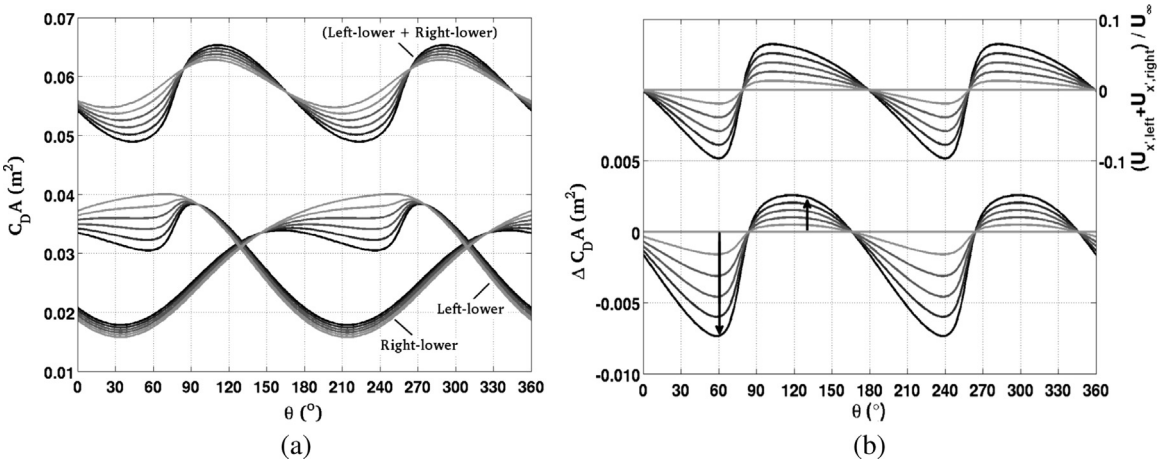

Fig. 16. (a) Aerodynamic drag area simulated on the lower leg for various reduced pedalling frequencies. (b) Lines plotted with respect to the left-hand axis show the variation in $C_DA_{lowerleg}$ from static lower leg conditions. The asymmetry in the pumping motion of the lower left/right legs, defined by $(U_{x',left} + U_{x',right})_{lowerleg}$, is plotted with respect the right-hand axis. (Note that the colours of the lines have been graduated from light to dark to mark simulated C_DA results for increasing reduced pedalling frequencies, where k = 0, 0.023, 0.046, 0.069, 0.092, 0.115.)

perpendicular component of the rotational velocity from both left and right upper legs. Fig. 15(b) shows, for $l=L$ (the knee joint), that this measure of the asymmetry in the motion of the upper legs can account for the difference in the simulated C_DA from static to pedalling legs $\Delta C_DA = (C_DA_{static} - C_DA_{\theta})_{upper\ leg}$.

A similar analysis can also be used to show how asymmetries in the motion of the lower legs contribute to the dependence of C_DA on cadence. Fig. 16(a) shows that there are phases of the crank cycle where the lower leg rotational and translational velocity components will either increase or decrease the drag area acting on left and right lower legs. This is primarily attributed to the asymmetry in the oscillating motion of the lower legs in the upstream and downstream directions. This asymmetry is described by the sum of the horizontal translational component of velocity of the left and right lower legs (referenced about the knee joint) and is plotted in Fig. 16(b). As a general rule, if the relative translational velocity $(U_{x',left} + U_{x',right})_{lowerleg}$ is positive, the total drag acting on the left/right lower legs increases. If $(U_{x',left} + U_{x',right})_{lowerleg}$ is negative, the total lower leg C_DA decreases. As a result of this, the difference in the total lower leg C_DA from quasi-steady to moving legs, also depicted in Fig. 16(b), grows with the asymmetry in the back and forth pumping motion. The amplitude of the pumping asymmetry grows with increasing cadence and has a 'stretching' effect on the variation in the total simulated drag area about the mean. When these asymmetries are considered together with the asymmetry in the motion of the upper legs, they provide one explanation for why reductions in C_DA are observed around the high-drag quasi-steady leg positions (75°, 255°) and why the peak C_DA values are shifted towards later stages in each half of the crank cycle with increasing cadence.

4. Conclusion

The streamwise vortical flow structures and velocity deficit in the wake of a full-scale pedalling cyclist model have been mapped through wind-tunnel experiments for a range of reduced pedalling frequencies. Up to elite-level pedalling cadences (100 RPM), phase-averaged velocity fields reveal the coherent large-scale wake flow structures as they pass through a downstream plane. The primary wake features, i.e., the upper and lower hip vortices, as well as smaller-scale flow structures (ankle-calf vortices) are found to be consistent across all pedalling frequencies tested and agree well with results from previous quasi-steady investigations into the flow topology of cyclist wakes. Overall, very little variation in the wake flow structure of both the characteristic symmetrical (low-drag) and asymmetrical (high-drag) flow regimes was observed comparing quasi-steady (static-legs) and phase-averaged moving-leg flow fields.

Both time-averaged and mean pedal-stroke phase-averaged forces suggest that there are limited gains in aerodynamic performance available through adjusting cycling cadence with a conventional pedal stroke. However, the results and analysis of phase-averaged force estimates indicate that gains in aerodynamic performance may possibly be achieved by adopting a non-uniform pedalling rate over the pedal stroke, or possibly a non-circular pedal stroke motion. A simple quasi-static force model was able to show how asymmetries in the rotational rates, and back and forth pumping motion of the legs, which grow with the pedalling rate, can partially account for the observed dependence of measured phase-averaged C_DA values on the cycling cadence. It appears that further gains in aerodynamic performance can be achieved by favouring certain asymmetries that occur in the relative pumping motion between the left and right legs.

Appendix A. Supplementary material

Supplementary data associated with this article can be found in the online version at http://dx.doi.org/10.1016/j.jfluidstructs.2016.05.007.

References

Achenbach, Elmar, 1971. Influence of surface roughness on the cross-flow around a circular cylinder. J. Fluid Mech. 46 (02), 321–335.

Barry, N., Burton, D., Sheridan, J., Thompson, M., Brown, N.A., 2014. Aerodynamic performance and riding posture in road cycling and triathlon. J. Sports Eng. and Technol. Part: P, 1–11, http://dx.doi.org/10.1177/1754337114549876.

Betz, A., 1925. A method for the direct determination of profile drag. Z. Flugtech. Motorluftschiffahrt 16, 42–44.

Brune, G.W., 1994. Quantitative low-speed wake surveys. J. Aircr. 31 (2), 249–255.

Chen, J., Haynes, B.S., Fletcher, D.F., 2000. Cobra probe measurements of mean velocities, Reynolds stresses and higher-order velocity correlations in pipe flow. Exp. Therm. Fluid Sci. 21 (4), 206–217.

Clanet, Christophe, 2015. Sports ballistics. Annu. Rev. Fluid Mech. 47, 455–478.

Crouch, T.N., Burton, D., Brown, N.A.T., Thompson, M.C., Sheridan, J., 2014a. Flow topology in the wake of a cyclist and its effect on aerodynamic drag. J. Fluid Mech. 748, 5–35.

Crouch, T.N., Burton, D., Thompson, M.C., Martin, D.T., Brown, N.A.T., Sheridan, J., 2014b. A phase-averaged analysis of the pedalling cyclist wake. In: Proceedings of the 19th Australasian Fluid Mechanics Conference, Melbourne, Victoria, Australia, pp. 1–4.

Defraeye, T., Blocken, B., Koninckx, E., Hespel, P., Carmeliet, J., 2010. Aerodynamic study of different cyclist positions: Cfd analysis and full-scale wind-tunnel tests. J. Biomech. 43 (7), 1262–1268.

Defraeye, Thijs, Blocken, Bert, Koninckx, Erwin, Hespel, Peter, Carmeliet, Jan, 2011. Computational fluid dynamics analysis of drag and convective heat transfer of individual body segments for different cyclist positions. J. Biomech. 44 (9), 1695–1701.

Ericson, Mats O., Nisell, Ralph, Arborelius, Ulf P., Ekholm, Jan, et al., 1986. Power output and work in different muscle groups during ergometer cycling. Eur. J. Appl. Physiol. Occup. Physiol. 55 (3), 229–235.

Griffith, M.D., Crouch, T., Thompson, M.C., Burton, D., Sheridan, J., Brown, N.A.T., 2014. Computational fluid dynamics study of the effect of leg position on cyclist aerodynamic drag. J. Fluids Eng. 136 (10), 101105.

Hackett, J.E., Sugavanam, A., 1984. Evaluation of a Complete Wake Integral for the Drag of a Car-like Shape. Technical Report, SAE Technical Paper.

Hooper, J.D., Musgrove, A.R., 1997. Reynolds stress, mean velocity, and dynamic static pressure measurement by a four-hole pressure probe. Exp. Therm. Fluid Sci. 15 (4), 375–383.

Hosoi, A.E., 2014. Drag kings: characterizing large-scale flows in cycling aerodynamics. J. Fluid Mech. 748, 1–4.

Karabelas, S.J., Markatos, N.C., 2012. Aerodynamics of fixed and rotating spoked cycling wheels. J. Fluids Eng. 134 (1), 011102.

Katz, Joseph, 2006. Aerodynamics of race cars. Annu. Rev. Fluid Mech. 38, 27–63.

Kusunose, Kazuhiro, 1997. Development of a Universal Wake Survey Data Analysis Code. AIAA Paper (97-2294).

Maskell, E.C., 1963. A Theory of the Blockage Effects on Bluff Bodies and Stalled Wings in a Closed Wind Tunnel. Technical Report, DTIC Document.

Maskell, E.C., 1973. Progress Towards a Method for the Measurement of the Components of the Drag of a Wing of Finite Span. Procurement Executive, Minister of Defence.

Schlichting, Herrmann, Gersten, Klaus, 2000. Boundary-Layer Theory. Springer Science & Business Media, Berlin.

Wei, T., Mark, R., Hutchison, S., 2014. The fluid dynamics of competitive swimming. Annu. Rev. Fluid Mech. 46, 547–565.

Wu, James Chen-Yuan, 1982. A Generalized Wake-Integral Approach for Drag Determination in Three-Dimensional Flows.

Zhou, J., Adrian, R.J., Balachandar, S., Kendall, T.M., 1999. Mechanisms for generating coherent packets of hairpin vortices in channel flow. J. Fluid Mech. 387 (1), 353–396.

Zhou, Y., Antonia, R.A., 1992. Convection velocity measurements in a cylinder wake. Exp. Fluids 13 (1), 63–70.